nature portfolio

https://doi.org/10.1038/s41565-021-00940-1

Supplementary information

Voltage control of ferrimagnetic order and voltage-assisted writing of ferrimagnetic spin textures

In the format provided by the authors and unedited

Voltage control of ferrimagnetic order and voltage-assisted writing of ferrimagnetic spin textures

Mantao Huang, Muhammad Usama Hasan, Konstantin Klyukin, Delin Zhang, Deyuan Lyu, Pierluigi Gargiani, Manuel Valvidares, Sara Sheffels, Alexandra Churikova, Felix Büttner, Jonas Zehner, Lucas Caretta, Ki-Young Lee, Joonyeon Chang, Jian-Ping Wang, Karin Leistner, Bilge Yildiz and Geoffrey S. D. Beach

- Supplementary Information -

I. Composition of GdCo

We prepared Ta(4 nm)/Pd(6 nm)/Gd_xCo_{100-x}(6 nm)/Pd(10 nm) films with x = 39.3, 41.6, 43.8, 45.7, and 46.7. The H_c and polarity of MOKE hysteresis loops are shown in Figure S1. The coercivity diverges and the loop polarity inverts at $x \approx 44$, which corresponds to the compensation composition at room temperature. We estimate the composition of the samples in the main text to be $Gd_{45}Co_{55}$ based on measured H_c and the MOKE loop polarity.

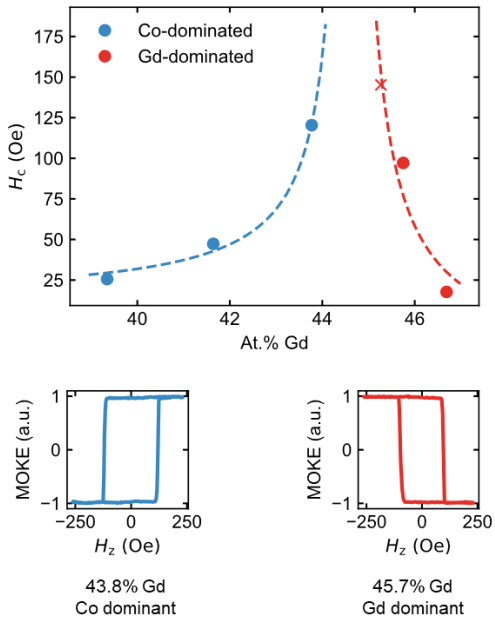

Figure S1 | a, H_c and MOKE loop polarity versus Gd atomic percent of GdCo. **b,** MOKE hysteresis loops at x = 43.8 and x = 45.7.

II. Hydrogen sourced from hydrolysis of water in the gas environment

As discussed in Ref[1–3], in metal(anode)/GdO_x/Au stacks, by applying a positive gate voltage $V_G \gtrsim 1.2V$ to the top Au and grounding the bottom metal layer, water from the ambient is split at the top electrode forming oxygen and protons. The protons are driven by electric field towards the bottom electrodes where they recombine with electrons and get loaded into the bottom electrode. The mechanism was supported by X-ray absorption spectroscopy measurements[1]. Figure S2 shows the processes involved when a positive V_G is applied for the device structures used in this manuscript.

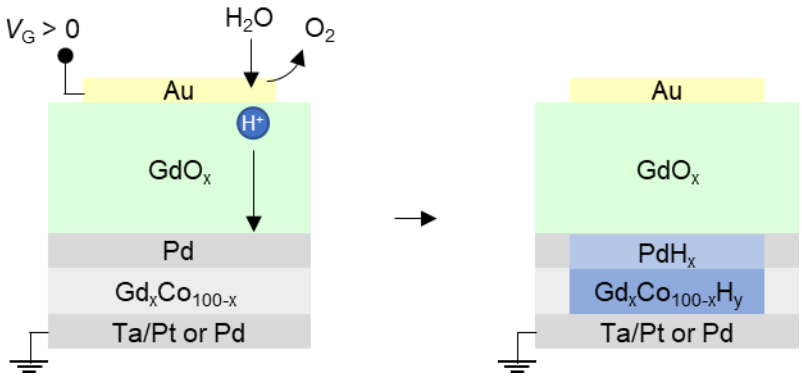

Figure S2 | Schematic illustration of water splitting and hydrogen pumping by applying a positive V_G

The electrode reactions involved during hydrogen loading are:

$$\mathrm{Anode(Au)}: 2H_2O \rightarrow 4H^+ + O_2 + 4e^- \quad \text{(S1)}$$

$$\mathrm{Cathode(Pd)}: Pd + xH^+ + xe^- \rightarrow PdH_x \quad \text{(S2)}$$

$$\mathrm{Cathode(GdCo)}: Gd_xCo_{100-x} + yH^+ + ye^- \rightarrow Gd_xCo_{100-x}H_y \quad \text{(S3)}$$

To support the processes described above, we experimentally show the critical role of water vapor in voltage induced hydrogen loading. Experiments were carried out to study the effect of different gas environments. Five devices with the same device structure fabricated in the same batch were used in the study. The polar MOKE loops of the devices in the virgin state were measured. Then V_G = +3 V was applied to one device for 180 s in ambient, and the same V_G was applied to another device for 180s in vacuum (<10^{-3} Torr). The other three devices were first placed in a vacuum chamber. After the vacuum level reached

10^{-3} Torr, dry nitrogen, dry oxygen, and wet nitrogen were introduced to the chamber for each device respectively. After the pressure level reached 20 Torr, V_G = +3 V was applied to each device for 180 s, and then the devices were left open circuit. MOKE hysteresis loops of these devices were taken again after the voltage applications. The results are shown in Figure S3. Inversion of hysteresis loop polarity was only observed in gas environment with water vapor and the hysteresis loops of the rest of the devices did not show observable changes. The critical role of water vapor in the gating process supports the water splitting and hydrogen injection mechanism.

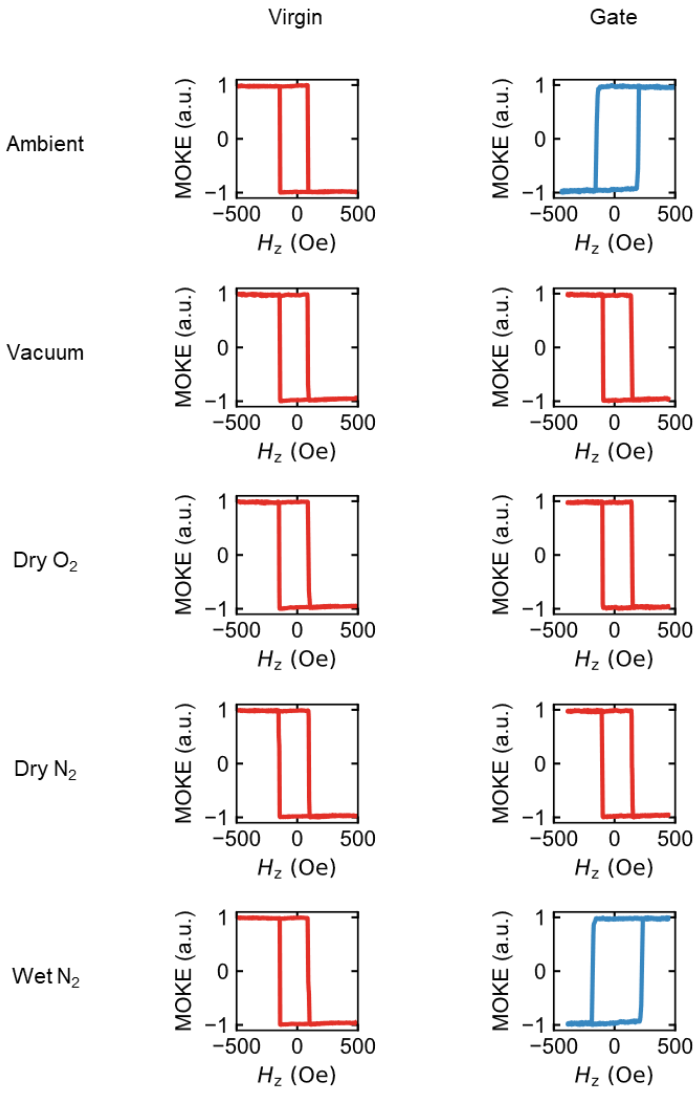

Figure S3 | MOKE hysteresis loops before and after applying V_G = +3 V for 180 s under different gas environments

III. Progression of R_{AHE} as a function of cycle number as the device was cycled between Gd and Co-dominant state

Figure S4 shows the progression of the magnitude of R_{AHE} monitored for a device with the same structure as devices shown in Figure 4 in the main text, as it was cycled between Gd and Co-dominant states. Here $|\Delta R_{AHE}|$ is the amplitude of R_{AHE} determined from hysteresis loops acquired after each gate voltage application. The AHE amplitude in both the Gd and Co dominated states was found to be very stable throughout the cycling process of >10,000 cycles.

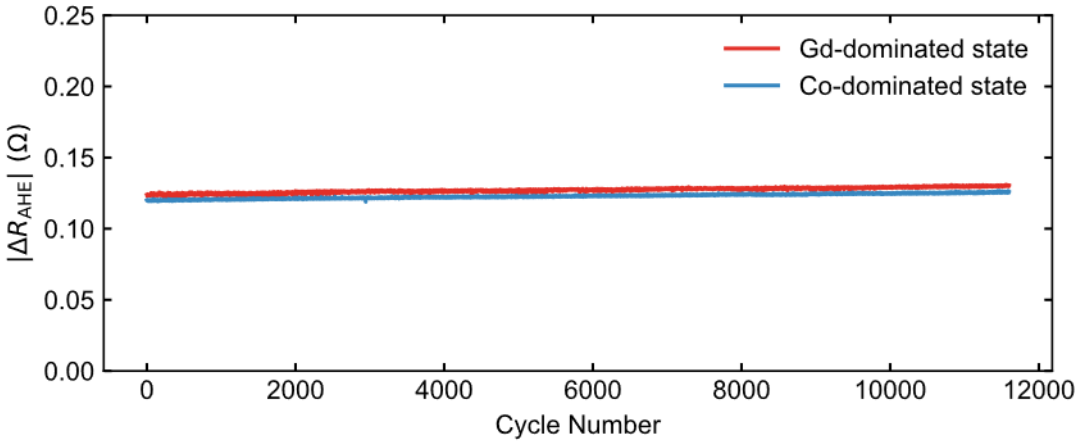

Figure S4 | Progression of $|\Delta R_{AHE}|$as a function of cycle number as the device was cycled between Gd and Co-dominated state

There is a small drift in the AHE amplitude over time, which is likely an artifact. In the Hall effect measurements, a constant amplitude voltage source was used to drive the Hall cross, and the sense current I_s was determined using the measured resistance of the device under test. Both temperature and contact resistance drift during the measurement could contribute to the observed drift in the Hall voltage amplitude and the corresponding value of R_{AHE} computed as $R_{AHE}=V_{AHE}/I_s$. Nonetheless, the drift is only a few percent at most.

IV. Toggling of the zero-field sign of the AHE from GdCo layer

V_G = +2.5 V(-1.6 V) were applied to the devices with FePd stray field biasing layer in order to switch the dominant sublattice to Co (Gd). The AHE signal of GdCo was measured in a differential manner because

the signal amplitude is small and the drift of lock-in signal due to impedance fluctuations over time is on the same order of magnitude as the actual signal. For each measurement, a small probing field pulse (-240 Oe, 0.4s) was applied to switch the GdCo sublattices while the AHE signal was recorded. Figure S5 shows two example sets of measurement for Cycle #2 in Figure 5e. The field value (-240 Oe) was chosen so that the FePd layer is not affected by the field and the GdCo layer is switched so that a differential signal from GdCo can be captured. The AHE signal is finally calculated by $R_{\mathrm{AHE}} = \frac{\Delta V_{\mathrm{AHE}}/2}{I_{\mathrm{drive}}}$, where ΔV_{AHE} is the V_{AHE} value before the field pulse subtracted by its value when the field pulse is on, and I_{drive} is the driving current for the Hall cross. Note that such probing scheme does not assist the field-free-switching process because as shown in the figures, after the probing field pulse, the sublattice orientation always restored to the same configuration as before the field pulse spontaneously. The spontaneous restoration of sublattice orientation also indicates that the net magnetization of the GdCo is pinned by the stray field from FePd and the system is robust against external fields.

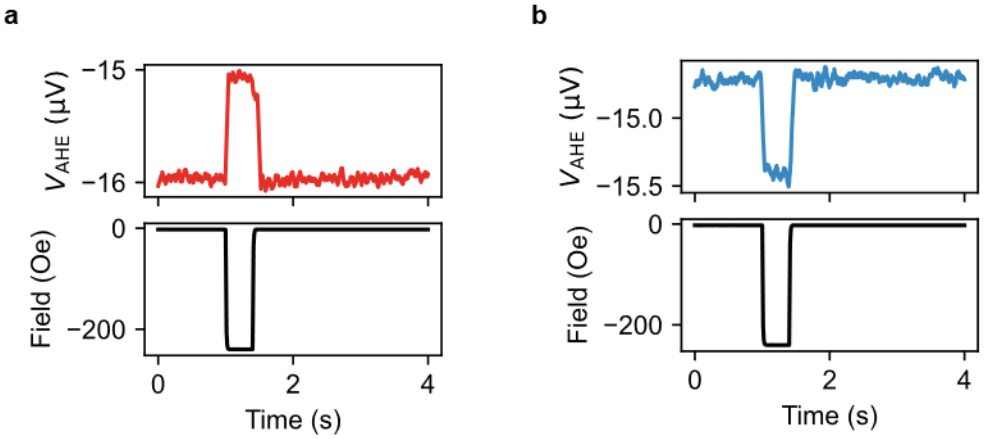

Figure S5 | Differential R_{AHE} measurement scheme and an example set of results for Cycle #2 in main text Figure 5e, when the dominant sublattice was switched to Gd (**a**), and when dominant sublattice was switched to Co (**b**).

V. Wide field MOKE contrast images of skyrmion generator track when current is injected from right to left

Figure S6 shows the MOKE contrast images of the skyrmion generator after the initiation sequence described in the main text, after each of a series of current pulses injected laterally while holding a small out-of-plane stabilizing field. The current pulses were injected from right to left, which is reversed comparing to the current injected in Fig. 6 in the main text, and the skyrmion bubble also moved towards the reversed direction as expected.

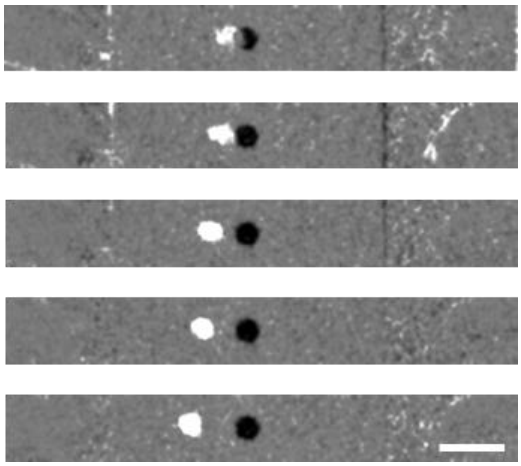

Figure S6 | Sequence of wide field MOKE contrast images showing the movement of the generated skyrmion bubbles with lateral current pulses injected from right to left. Scale bar, 100 μm

VI. Details on static DFT calculations

We investigate the stability of hydrogen absorption sites in $GdCo_2$ structure and the effect of hydrogen incorporation on magnetic moments of adjacent metal atoms as shown in Figure S7 a-d. DFT calculations indicate that H absorption in 3Co1Gd interstitials is the most energetically favorable with the energy of -0.27 eV, 4Co tetrahedral interstitials are less favorable with absorption energy of -0.24 eV, while absorption of H in 2Co2Gd sites is energetically unfavorable. As it is seen from Figure S7, magnetic moment on Co atoms varies in the range of 1.2-1.6 μ_B depending on H absorption site and vicinity of metal ions, while magnetic moment on Gd remains almost unchanged for the considered configurations.

Absorption energy was calculated as following: $E_{ads} = E_{GdCo2Hx} - E_{GdCo2} - x \cdot E_{H2}$, where $E_{GdCo2Hx}$ – total energy of $Gd_8Co_{16}H$; E_{GdCo2} – total energy of Gd_8Co_{16}; E_{H2} – total energy of H_2.

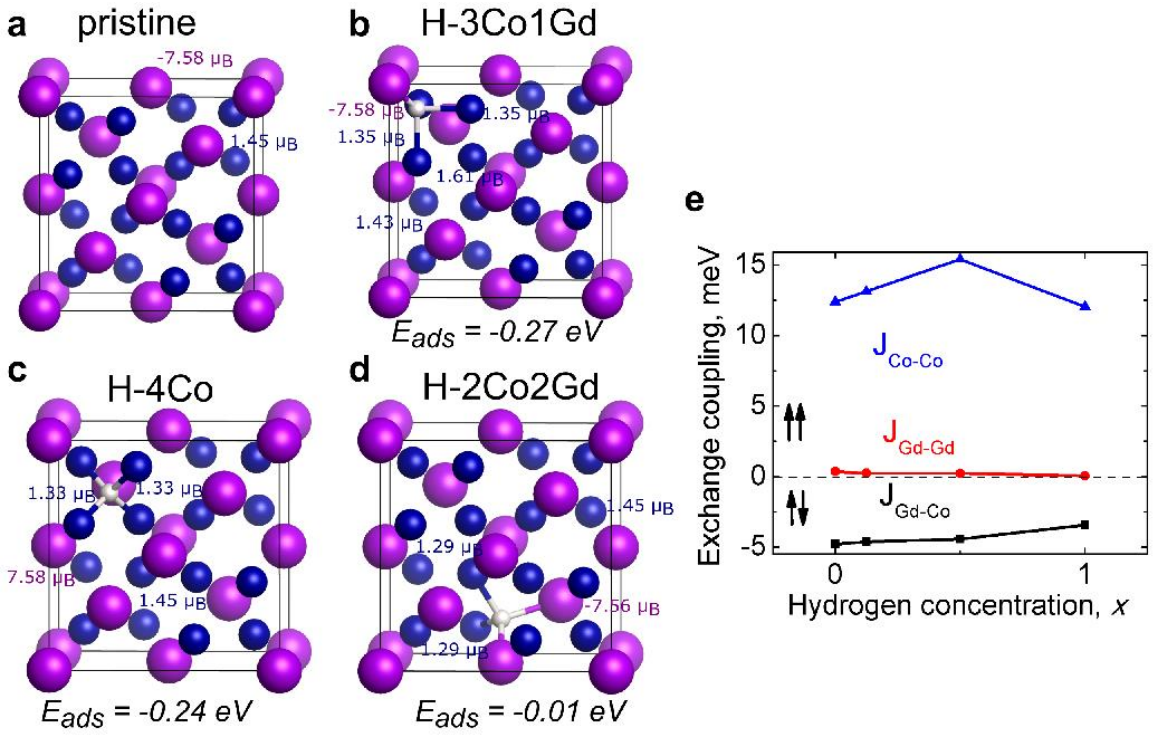

Figure S7 | a, Cubic $GdCo_2$ (C15 laves) structure with the three possible types of interstitial tetrahedral sites labeled as 3Co1Gd – **b**, 4Co – **c**, and 2Co2Gd – **d**. Purple spheres represent Gd, blue spheres represent Co, small white spheres are H atoms. Magnetic moments on Co and Gd atoms are shown in blue and purple, correspondingly. **e**, Evolution of exchange coupling constants upon $GdCo_2H_x$ hydrogenation; the desired H/M ratio was generated by the introduction of H atoms into the 4Co interstitial sites.

Figure S7e shows the evolution of exchange coupling constants upon hydrogen incorporation into 4Co interstitials, while the corresponding figure for 3Co1Gd interstitials is shown in the manuscript (see Figure 3b). For both types of hydrogen interstitials, we observe a weakening of antiferromagnetic exchange coupling between Co and Gd sublattices upon hydrogen insertion, which leads to the reduction of M_{Gd} and dominant sublattice switching.

Our DFT calculations revealed that second neighbor exchange coupling constants (J) are almost zero (considerably smaller than J for the nearest neighbors), which means that magnetic order is mostly determined by the local structure. This means that there should not be a substantial difference between

amorphous and crystalline phases in terms of the effect of H on the exchange constants. H atoms will also occupy either tetrahedral or octahedral metal pores even in an amorphous structure, and the effect on exchange coupling is local. Therefore, one would not expect that the qualitative behavior of amorphous and crystalline phases will be different.

References

1. Tan, A. J. *et al.* Magneto-ionic control of magnetism using a solid-state proton pump. *Nat. Mater.* **18**, 35–41 (2019).

2. Tan, A. J. *et al.* Hydration of gadolinium oxide (GdOx) and its effect on voltage-induced Co oxidation in a Pt/Co/GdOx/Au heterostructure. *Phys. Rev. Mater.* **3**, 064408 (2019).

3. Huang, M. *et al.* Voltage-gated optics and plasmonics enabled by solid-state proton pumping. *Nat. Commun.* **10**, 5030 (2019).